PCCP

ROYAL SOCIETY OF CHEMISTRY

PAPER

Cite this: *Phys. Chem. Chem. Phys.*, 2021, **23**, 7247

Lattice dynamics in the conformational environment of multilayered hexagonal boron nitride (h-BN) results in peculiar infrared optical responses†

Luigi Cigarini, * Michal Novotný and František Karlický *

Received 29th November 2020,
Accepted 1st March 2021

DOI: 10.1039/d0cp06188c

rsc.li/pccp

Stacking mismatches in hexagonal boron nitride (h-BN) nanostructures affect their photonic, mechanical, and thermal properties. To access information about the stacked configuration of layered ensembles, highly sophisticated techniques like X-ray photoemission spectroscopy or electron microscopy are necessary. Here, instead, by taking advantage of the geometrical and chemical nature of h-BN, we show how simple structural models, based on shortened interplanar distances, can produce effective charge densities. Accounting these in the non-analytical part of the lattice dynamical description makes it possible to access information about the composition of differently stacked variants in experimental samples characterized by infrared spectroscopy. The results are obtained by density functional theory and confirmed by various functionals and pseudopotential approximations. Even though the method is shown using h-BN, the conclusions are more general and show how effective dielectric models can be considered as valuable theoretical pathways for the vibrational structure of any layered material.

1 Introduction

Layered materials are widely studied due to their ability to form stable single-layer (2D) crystals. Exotic and unexpected properties like astounding electronic conductivity or unusual optical response[1] can arise in some materials when reduced to their 2D forms.[2] Hexagonal boron nitride (h-BN) is considered a counterpart to graphene as its structure is almost identical, yet h-BN is a semiconductor with a relatively large electronic (6.08 eV)[3–5] and optical (5.69 eV)[4–6] band gap in bulk. Single h-BN layers can be efficiently used as dielectric layers in graphene nanostructures, electronics, or for lubrication, or directly replace other materials for high-temperature applications.[7] The crystalline structure of h-BN has been addressed in previous theoretical studies,[4,8–16] yet the question of stability for different possible stacking orders has not been answered to a satisfactory level.[4,14,15,17,18]

From a geometrical point of view, it is clear that a wide variety of stacking arrangements are possible for the displacement of contiguous planes and several of them have been reported experimentally.[19–24] Five possible arrangements are shown in Fig. 1.

The AA′ and AB types of stacking orders have been observed by atomic resolution imaging[19,24] and are known to be stable. H-BN is generally considered to be in the AA′ stacking. New experimental routes[22] recently showed how to produce a purely AB stacked material. AA and A′B have been reported by theoretical calculations to be unstable,[14] nevertheless they have been found in traces in experimental measurements,[20,21] while at the same time the actual amount of AB′ stacking in h-BN samples remains unclear.[14,18,23,25,26] The uncertainty is increased by the wide variability in experimental data obtained from infrared optical responses,[27–33] Raman optical activity and[27,34–36] photoluminescence spectroscopy.[37–39] This may be due to a variety of different sources (among others: possible poly-crystallinity, presence of amorphous regions, impurities), including stacking defects and variability in the amount of differently stacked regions in the probed specimens. Although many stacking combinations are possible, only two[27] or three[40] of them have been considered in different theoretical studies related to the interpretation of

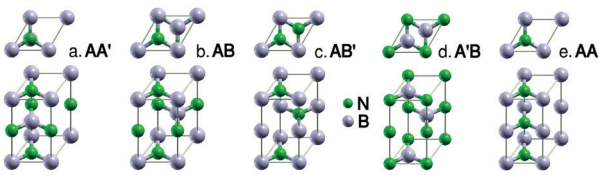

Fig. 1 Five different stacking orders in hexagonal boron nitride (top and axonometric views).

Department of Physics, Faculty of Science, University of Ostrava, 701 03 Ostrava, Czech Republic. E-mail: luigi.cigarini@osu.cz, frantisek.karlicky@osu.cz

† Electronic supplementary information (ESI) available. See DOI: 10.1039/d0cp06188c

experimental results. Until now, there has been no reported simple way to unravel the stacking composition of samples.

An accurate description of the lattice dynamics and stacking composition of bulk h-BN would produce a better explanation of experiments[41] and might contribute to achieving higher control over the crystalline aspects of the produced samples, as well as finer tuning of the final properties of interest, a precise value of thermal conductivity[42–45] or optical and photonic response,[26,46–49] and control over the materials in nanostructuring processes.[36,41,50–52] An important example of how stacking behaviour may have a practical impact is in the recent discovery that the local strain of the h-BN lattice framework is related to the single photon quantum emission properties.[53] But, specifically, a great anisotropy between the parallel and perpendicular plane dielectric constants has been reported for bulk h-BN in theoretical[12] and experimental studies,[27] yet theoretical models failed to reproduce the measured results.[13] As we thoroughly describe in Section 2.3, the different nature of the physical forces involved (covalent in-plane interactions and the inter-plane van der Waals forces) makes striving for a uniform theoretical interpretation extremely difficult.

Theoretical descriptions of the lattice dynamics of solids usually utilize density functional theory (DFT).[54] Particularly, local density approximation (LDA) exchange–correlation (xc) functionals are often reported to be the best compromise for a consistent description of h-BN,[17,40,55,56] nevertheless, satisfactory theoretical interpretation has not yet been reported on the paradoxical success of LDA. Janotti *et al.*[57] performed all electron DFT calculations on bulk h-BN. The comparison of LDA results with the more sophisticated generalized gradient approximation (GGA) did not produce substantial improvement in the interpretation of the stacking interaction. The same conclusion was reported by Mosuang *et al.*[40] with the use of norm-conserving (NC) pseudopotential (PP) approximations. LDA theoretical implementations have produced results in a relatively satisfactory agreement with experimental values for the calculations of lattice constants, bulk moduli and cohesive energies of this material by employing any norm-conserving (NC),[12,40] ultrasoft (US)[11] or projector augmented-wave (PAW)[58] pseudopotential (PP) approximations. Kim *et al.*[59] reported a significant improvement in the calculation of lattice constants using Troullier–Martins[60] NC PP, generated within the GGA correction, but implemented in an LDA xc functional theory. As a consequence, the lattice dynamics of bulk h-BN and the issue of relative stability of the different stacking orders until the present work, has been examined mainly by LDA approaches, employing US PP[13,14,61,62] and NC PP.[8,17,63] GGA approaches[64] never showed noticeable improvement before. A new promising candidate to resolve these issues, the strongly constrained and appropriately normed (SCAN)[65,66] functional has been advanced to deal efficiently with diversely bonded materials (including covalent and van der Waals interactions).

In this work, we present a comprehensive study of the lattice dynamics of bulk h-BN comparing five different possible stacking variants (within different levels of DFT functionals, PPs and vdW corrections). We employ an original methodology, based on a separate description of the analytical (inter-atomic force constants) and non-analytical parts (Born effective charges and dielectric tensors) of the dynamical matrix and we propose a simple, but effective, approach for the non-analytical calculations. Our chosen methodology of utilizing different levels of theory (LDA, GGA, SCAN, US-PP, NC-PP, and PAW-PP) is not merely empirical, but arises from a careful consideration of the physics responsible for nuclear motion and dielectric dynamics. Using the available experimental data (without insights into their conformational composition), we are able to assess the quality of our calculations (Section 3.3) and derive a semi-empirical method (Section 3.4) which is potentially able to determine the conformational composition of the given samples. Overcoming the possible experimental difficulties, future developments (comprehensive data sets and powerful theoretical implementations) could permit a numerical shift in the present model and result, then, in an accurate interpretation of the measurements.

2 Methods

2.1 Lattice dynamics

We first analyzed the structure of the considered systems by means of well established phonon dynamical theories, within the theoretical scheme of the harmonic approximation. The vibrational movements, in periodic systems, are defined by a wave vector $\mathbf{q}$ and a mode number ν. For each wave vector and mode it is possible to determine energy (vibrational frequency $\omega_\nu(\mathbf{q})$) and displacements vectors $u^\alpha_{s,\nu}(\mathbf{q})$ by solving the phononic eigenvalue problem[67–69] deriving the interatomic force constants (IFC) by means of a finite displacements (FD) method.

This analytical approach is not sufficient to account for long-range Coulombic forces which originate in real crystal structures and give rise to longitudinal-transverse optical (LO-TO) mode splitting. It is necessary to introduce a non-analytical (NA) correction term in the computed dynamical matrices. This approach was first derived by Cochran and Cowley[70] based on the Born and Huang[71] theoretical framework, successively adapted by Pick *et al.* in the form which is currently implemented in the modern theories.[13,72] It is based on a separation of the dynamical matrix into two different terms. The eigenvalue problem can then be reformulated, in real space, for the α direction (without noting the explicit dependence over $\mathbf{q}$ of ω, W and N):

$$\omega_\alpha{}^2 W = \left(N + \frac{4\pi}{\varepsilon^{(\infty)}_{\alpha\alpha}} Z \delta_{\alpha\beta} Z^T \right) W, \tag{1}$$

where the W matrix contains the displacement vectors u_s of the atoms of mass μ_s (labeled by index s): $W^\alpha_\mathrm{s} = \sqrt{\mu_\mathrm{s}} \cdot u^\alpha_\mathrm{s}$. The N matrix contains information about the interatomic force constants (IFC) of the system: $N^{\alpha\beta}_{\mathrm{st}}(q) \propto \tilde{C}^{\alpha\beta}_{\mathrm{st}}(q)/(\sqrt{\mu_\mathrm{s}\mu_\mathrm{t}})$ where t is a second index for nuclei. $\tilde{C}^{\alpha\beta}_{\mathrm{st}}(q) = \sum_l \mathrm{e}^{-iqR_l} C^{\alpha\beta}_{\mathrm{st}}(R_l)$ is the analytical part of the dynamical matrix of the system. $C^{\alpha\beta}_{\mathrm{st}}(R_l)$ are the elements of the IFC, defined as:

$$C^{\alpha\beta}_{\mathrm{st}}(l,m) = \frac{\partial^2 E}{\partial u^\alpha_\mathrm{s}(l)\partial u^\beta_\mathrm{t}(m)}, \tag{2}$$

where E is the total energy of the system, R_l is the nuclear coordinates matrix in the l unit cell, l and m are indices of different unit cells. The explicit dependency of $C_{st}^{\alpha\beta}$ on couples of unit cell (l,m) is intended, in eqn (2), to account for numerical implementations of IFC calculation. In the NA part, the Z matrix ($Z_s^{\alpha\beta} = Q_s^{\alpha\beta}/\sqrt{\mu_s}$) contains elements of the Q matrix of the effective charges (later defined in eqn (6)).

Giannozzi *et al.*,[73] Ohba *et al.*[13,74] and Gonze *et al.*[75] obtained effective charges and dielectric tensors by density functional perturbation theory (DFPT) and directly related them to the LO-TO splitting of the phononic modes and absorption activities. In a slightly different approach, here we consider the charges $Q_s^{*\alpha\beta}$[76] and dielectric tensors ε calculated by DFPT as numerical counterparts of the Q matrix elements and $\varepsilon^{(\infty)}$ matrices of fictitious systems (the problem is shifted to the ideal creation of them and understanding the underlying relation). By constraining the cell in a single direction (perpendicular to the BN planes), we propose the aforementioned systems and thereby approximate the dynamical behavior of the dielectric dispersion matrix.

2.2 Infrared optical response

Porezag *et al.*[77] applied the pioneering work of Wilson *et al.*[69] to derive an expression for the absorption activity of phononic modes. The infrared (IR) absorption activity of a mode ν is:

$$I_\nu^{\mathrm{IR}} = \frac{n\pi}{3c}\left|\frac{\partial \boldsymbol{\mu}}{\partial q}\right|_\nu^2, \tag{3}$$

where n is the particle density, c is the velocity of light and $\boldsymbol{\mu}$ is the electric dipole moment of the system. The expression is reformulated by defining the Born effective charges $Q_s^{*\alpha\beta}$[67]:

$$I_\nu^{\mathrm{IR}} = \sum_\alpha \left|\sum_{s,\beta} Q_s^{*\alpha\beta} u_{s,\nu}^\beta\right|^2. \tag{4}$$

Our use of DFPT in the calculation of the NA dynamical parameters (*e.g.* $Q_s^{*\alpha\beta}$, which also takes part, eqn (4), in the IR activity) differs conceptually from how the theory was originally conceived. Here we propose it as a numerical tool, which permits one to relate uniquely every (possibly fictitious) charge density function to an absorption spectrum. We point out that the Γ point eigenvectors of the IR active modes can be directly compared with the experimental peak frequencies, and we notice that a natural broadening of the spectral lines, in a Lorentz function shape, occurs due to the finite lifetime of the phonon collective excitations as a consequence of scattering processes.

2.3 Semi-empirical description of the dielectric dynamics

In this paragraph, we present a short qualitative description that introduces our original approach. We begin with a molecular orbital (MO) depiction of the multilayered h-BN system, where the sp^3 orbitals related to the nitrogen atoms bear an electronic "lone pair". In this picture, the configuration of the orbitals and the relevant electronic clouds resonate between two limit forms in the upper and lower sides of the h-BN plane (ammonia-like inversion movement, see Fig. 2). Strong instantaneous dipoles are responsible for the van der Waals stacking interaction, in a continuous fluctuation of the charge density (and dielectric dispersion) between the two sides of the h-BN plane.

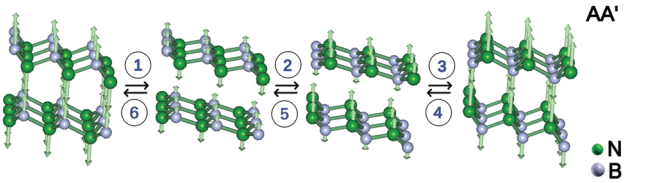

Fig. 2 Four different dynamical "snapshots" of the IR active A_{2u} vibrational mode of the AA′ configuration of h-BN (periodic movement in time is indicated by numbers and black arrows), which correspond to an ammonia-like inversion movement. Green arrows indicate the direction and magnitude of the displacement eigenvectors of the atom from its equilibrium position.

Cochran and Cowley[70] elegantly derived the following relation between the fluctuations of the dielectric dispersion involved in a vibrational mode related to the lattice dynamics of it (the ratio on the left side of eqn (5) between the frequencies ω_ν of phonons and dielectric dispersion frequencies Ω_ν) and the quotient of two dielectric constants of the system (on the right side of eqn (5)):

$$\prod_{\nu=4}^{3n}\left(\frac{\omega_\nu^\alpha}{\Omega_\nu}\right)^2 = \frac{\varepsilon_{\alpha\alpha}^{(0)}}{\varepsilon_{\alpha\alpha}^{(\infty)}}, \tag{5}$$

where ν is the index denoting different normal vibrational modes, n is the total number of atoms in the asymmetric unit, α is a space direction ($x \vee y \vee z$), and $\varepsilon^{(\infty)}$ and $\varepsilon^{(0)}$ are respectively the high frequency and static dielectric tensors. Recall that the high frequency dielectric tensor $\varepsilon^{(\infty)}$ depends only on the electronic susceptibility, *i.e.* just on charge density fluctuations, while the static dielectric tensor $\varepsilon^{(0)}$ depends also on the lattice dynamics.[70,71]

Ideally, two distinct values of frequency, ω_ν and Ω_ν, could be associated to a normal mode (eqn (5)), but in a mode with zero component of polarization in the α direction $\Omega_\nu = \omega_\nu^\alpha$. However, the dielectric dispersion frequencies (rigorously defined also in ref. 70) could be thought of as the frequencies of vibration of a fictitious system in which the dielectric dynamics is reproduced exactly. The dielectric dynamics can be described as dependent on an ideal "apparent charge density" $\rho_{(Q)}(r)$, $r \equiv (x,y,z)$, acting in determining the effective polarization of the crystal.

Accounting for this idealization, the total polarization is composed, in addition to the simple electronic polarization, by an ionic term Q^TU:[70,71]

$$P^\alpha = \sum_s Q_s^{\alpha\beta} u_s^\beta + \chi^{\alpha\beta} E^\alpha, \tag{6}$$

where U is the matrix of the ionic displacements u_s^α, χ is the electronic susceptibility matrix, and E^α is the real space components of the macroscopic electric field vector. The Q matrix (dimension $3n \times 3$, where n is the total number of atoms in the unit cell) is an expression of the "apparent charge density" $\rho_{(Q)}(r)$. Understanding this relation ($\rho_{(Q)}(r) \rightarrow Q$) is one of the purposes of

this study (for which we propose DFPT as a numerical tool, applied to fictitious, shortened systems).

We note that a given geometrical configuration and ground state charge density produce a unique "apparent charge density" $\rho_{(Q)}(r)$. This means that not only two systems with different geometrical conformations, but even two systems with the same geometrical conformation and different ground state charge density distributions (*e.g.* calculated with different DFT xc functionals, or different pseudopotential approximations) can be thought of as simulating diverse systems or as simulating varying average phases in a charge density fluctuation process, like that involved in a phononic mode vibration (like the A_{2u}, qualitatively depicted in Fig. 2).

By shortening the c lattice parameter (orthogonal to the h-BN planes), we can produce systems in which the frequency of vibration of the dielectric dispersion $\Omega_\nu^{\text{fict.}}$ associated to the A_{2u} mode, approaches progressively the Ω_ν of the real system.[70] By determining an optimal shortening percentage, the uniquely produced $Q_s^{*\alpha\beta}$ and ε effectively model the Q matrix elements and $\varepsilon^{(\infty)}$ matrices of real systems (NA parameters of the dynamical matrices), respectively, *i.e.* reproduce the actual ratio between the intensities of the two IR active absorptions. This optimization can also be observed when looking at the charge densities, as seen in the Appendix: the "apparent charge density", in the hypothetical polar cones of nitrogen, of the optimally shortened fictitious system mimics the effective function $\rho_{(Q)}(r)$ of the real system.

2.4 Computational details

The calculations are performed by means of the Quantum Espresso (QE)[78] package and VASP code,[79–82] using a periodic density functional theory (DFT)[54] in a plane waves (PW) basis set.[78–83] We treat the exchange–correlation (xc) potential within the electronic Hamiltonian in different manners: Local Density Approximation (LDA),[84] Generalized Gradient Approximation (GGA)[85] in the well-known Perdew–Burke–Ernzerhof (PBE)[86] formulation and the recently proposed Strongly Constrained and Appropriately Normed (SCAN)[65,66] functional. We employ the Vanderbilt Ultrasoft (US) PP,[87] Troullier–Martins FHI Norm-conserving (NC) PP[60,88–91] methods and the Projector Augmented-Wave (PAW) method of Blöchl.[92] US and PAW PP, in spite of a lower cutoff value in the PW basis set and a sensible reduction of computational time, do not guarantee the conservation of the norm for the resulting wave functions in comparison with all electron calculations, especially outside the core–shell regions of atoms. This drawback could particularly affect properties like phonons, which involve the calculation of interactions at longer than optimal distances with respect to covalent bonds. For this reason, in some of our implementations, we recalculate the charge densities after each diagonalization step, using dramatically higher (8–20 times) values of cutoff for the PW (see values of $E_{\text{cut}}.\rho$ with respect to E_{cut}. in the ESI† (Table TSI)).

To account for the lack of DFT to properly calculate weak interactions such as the interplanar van der Waals forces, we supplemented our DFT with empirical dispersion correction methods: Grimme-D2[93] and D3 with Becke–Johnson damping (D3BJ)[94] methods, Tkatchenko-Scheffler method (TS)[95] as well as the SCAN + rVV10[96] functional.

For each method we performed structural relaxations and phonon dispersion calculations. The calculation parameters and methods are summed up in the ESI† (Table TSI). We employ different fitting techniques to extrapolate the optimal structural parameters and the resulting values used in subsequent calculations are reported too, in the ESI† (Table TSII). The IFC have been calculated, after geometrical optimization, by means of a FD approach. From here on, the symmetries of the structures have been imposed as reported in the ESI,† Table TSIII. For the FD self-consistent field (SCF) calculations we employed VASP in conjunction with the Phonopy code[97] and the PW and FD algorithms included in QE. The DFPT Born effective charges and DFPT dielectric tensors[13,73,74] (here numerical expressions of Q matrix elements and $\varepsilon^{(\infty)}$ matrices) are obtained setting a threshold for self-consistency of 1.36×10^{-12} eV. The reported IR spectra are calculated by applying a Lorentz broadening function to the absorption intensities of the vibrational modes in order to have a half width at half maximum of 10 cm^{-1}. We separately applied the broadening functions to the single phonon spectral lines.

The potential energy surfaces (PESs) presented in Fig. 3 and in the ESI† (Fig. S1) have been obtained by means of the QE package with single point SCF calculations. These have been performed on Monkhorst–Pack $8 \times 8 \times 8$ **k**-points grids, with a SCF convergence threshold of 1.36×10^{-7} eV and all the other parameters as reported in the ESI† (Table TSI). The PESs are calculated at the resolution of 60×60 single point calculations on shifted structures, spanning the x and y directions from -0.5 Å to 0.5 Å, originating in the five symmetrical points of Fig. 1.

3 Results and discussion

3.1 Stability of the different conformers

In Fig. 3 and in the ESI† (Fig. S1) we report potential energy surfaces (PESs) cuts calculated within a selection of different methods. The figures are generated by keeping the a and c lattice constants fixed, as obtained for the five symmetrical structures (reported in the ESI† [Table TSII]) and by displacing the atoms in the lattices with parallel sliding of contiguous h-BN planes with respect to each other. A detailed description of these results is given in the ESI.† The shapes of the PESs confirm the stability of the AA′ and AB symmetrical structures, which is backed up by the comparison of the total energies in Table 1.

Furthermore, the AB′ point is located in a prominently flat valley (or a soft groove in NC-SCAN and US-LDA). Although the AA′ configuration is easily reachable upon simple sliding, the AB′ stacking configuration seems to be metastable, leading to possible interpretations of the experimental data related to dynamical stability.[26,52] The metastability of AB′ is particularly

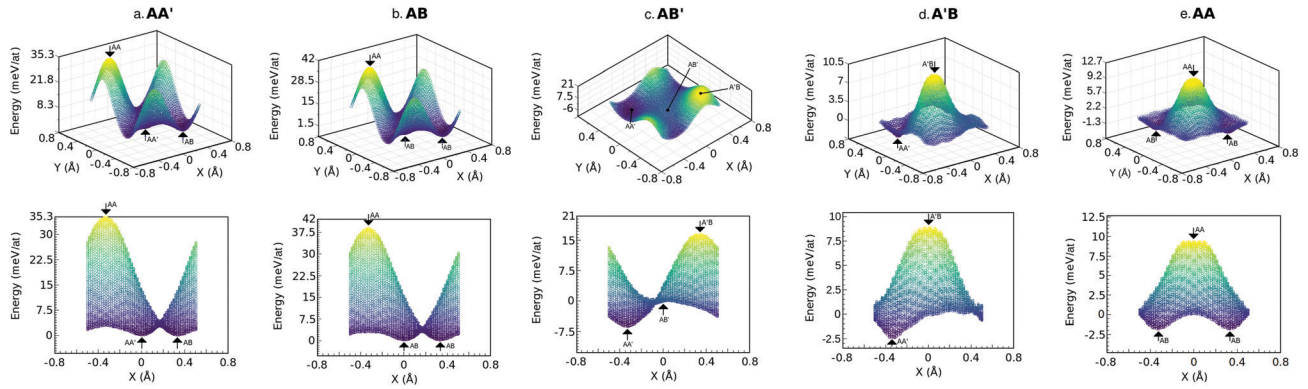

Fig. 3 Potential energy surfaces (PESs) cuts originating from the symmetrical points of all five stackings. The cell parameters have been kept constant (sourced from a full structural optimization). The PESs are calculated at the QE-PAW-PBE-D2 level of theory, by sliding of contiguous h-BN planes. Zero points in the energy scales correspond to the energies of the symmetrical structures.

Table 1 Relative energies (meV/at) of the various h-BN stacking configurations, with respect to the most stable configuration, calculated for every adopted method

		AA′	AB	AB′	A′B	AA
	Method	$P6_3/mmc$	$P3m1$	$P6_3/mmc$	$P6_3/mmc$	$P\bar{6}m2$
VASP	PBE-D2[a]	0.27	0.00	2.34	15.60	18.48
	PBE-D3BJ[a]	0.32	0.00	2.04	15.63	18.29
	PBE-TS[a]	2.80	0.76	0.00	15.98	17.72
	SCAN + rVV10[a]	0.42	0.00	2.49	17.86	21.02
QE	PBE-D2[a]	1.50	0.00	5.37	22.87	25.22
	LDA[b]	0.61	0.00	2.19	12.09	13.18
	PBE-TS[c]	0.22	0.00	1.81	9.26	9.96
	SCAN[c]	1.04	0.00	4.64	24.45	26.61

[a] Projector augmented-wave PP. [b] Ultrasoft PP. [c] Norm-conserving PP.

evident when examining the shape of the NC-SCAN PES reported in the ESI† (Fig. S1, uppermost panel).

We calculated the energetic dispersion of the vibrational modes for the five structures. We employed a wide selection of methods and we provide an extensive description of our results in the ESI.† While the Γ point frequencies of the AA′ variant are reported in Table 2, we report in the ESI,† all the data for the two other stable structures (Tables TSV and TSVI). A huge effort in interpretation is necessary, since, due to the nature of the systems and the elusive structure of the physical heterogeneity, the results obtained with different methods often lead to contrasting conclusions. Based on our analysis (see Section 3.3), we selected the most significant dispersion schemes and we report them in Fig. 4, confirming the stability of the stacking structures AA′, AB and AB′.

3.2 Vibrational structure

Two vibrational modes are IR active in h-BN (Fig. 5, described by the irreducible representations A_{2u} and E_{1u}), *i.e.* have $I_\nu^{IR} \neq 0$. The ratio between these two intensities can be informative about the microscopical nature of the system[99,100] and it is thoroughly studied here. Only one vibrational mode is active in Raman spectroscopy (E_{2g}). The frequency of vibration of this Raman active mode is degenerate with that of the IR active E_{1u} mode. Therefore, here we do not investigate Raman tensors.

In Fig. 6 we report the most significant (based on our analysis, see Section 3.3) vibrational spectra for the three stable stacking structures. The peak frequencies of the AB′ spectrum (1396 cm^{-1} and 751 cm^{-1}) have higher values with respect to the two other stable stackings: (1355 cm^{-1}, 724 cm^{-1} in AA′ and 1357 cm^{-1},

Table 2 Phonon frequencies at the Γ point (in cm^{-1}) for the AA′ stacking of h-BN as calculated by different theoretical approaches and software implementations and compared with experimental values taken from the literature. The same method used to calculate the IFC was used to obtain the NA except where it is specifically stated otherwise. The same theoretical data are provided for the AB and AB′ stackings in the ESI (Tables TSV and TSVI)

	VASP					QE					
Mode	PBE[a]	PBE-D2[a] (b)	PBE-D3BJ[a]	PBE-TS[a]	SCAN + rVV10[a]	LDA[b]	PBE-D2[a] (a)	PBE-TS[c]	PBE-TS[c] NA: PAW-PBE[a]	SCAN[c]	Experiment
E_{2g}[e]	47	47	46	37	47	50	60	48	48	51	51[34]
						51	63	53	53	51	
B_{1g}[e]	126	88	119	138	129	113	182	131	131	113	—
A_{2u}[d]	745	742	744	744	741	751	722	756	756	736	767–810[27–33]
B_{1g}[e]	797	793	797	800	795	811	791	810	810	797	—
E_{2g}[e]	1354	1359	1354	1356	1381	1384	1350	1345	1345	1367	1369–1376[27,34,35]
						1384	1351	1345	1345	1367	
E_{1u}[d]	1354	1359	1354	1356	1381	1384	1351	1345	1345	1367	1338–1404[27–33]
E_{1u}[d]	1589	1593	1589	1591	1629	1615	1591	1570	1573	1596	1616[27]

[a] Projector augmented-wave PP. [b] Ultrasoft PP. [c] Norm-conserving PP. [d] IR active modes. [e] Raman active modes.

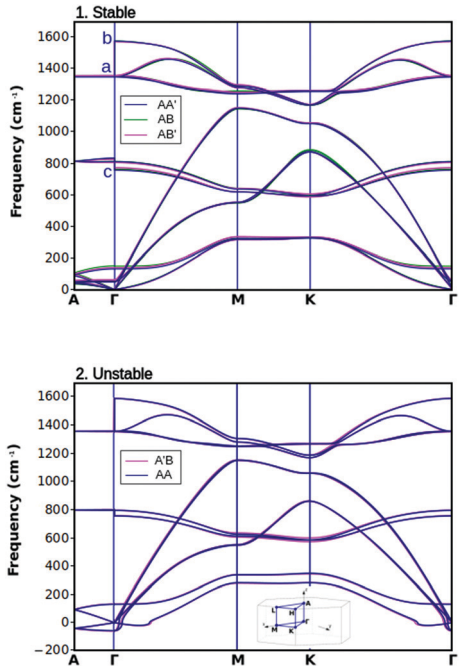

Fig. 4 Comparison of the phonon energy dispersions along high symmetry directions in the first Brillouin zone for five h-BN bulk systems.[98] IR or Raman active points are indicated as *a, b* and *c* and corresponding displacements are depicted in Fig. 5.

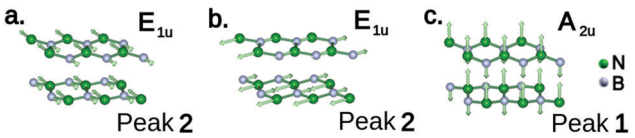

Fig. 5 (a–c) Graphical representations of the displacement eigenvectors (green vectors) in the AA′ stacked h-BN for three IR or Raman active modes at the Γ point (respectively indicated in Fig. 4).

733 cm^{-1} in AB). The ratio between the intensities of the two active absorptions is 12.129 in the AB′ structure which is considerably higher with respect to the other two systems (8.211 in AA′ and 9.500 in AB).

In Fig. 7 we extend our view and compare the ratios obtained with three different theoretical implementations. The same trend and peculiar behavior ($Ratio_{AB'} \gg Ratio_{AB} > Ratio_{AA'}$) are noticeable within all of the tested physical models. In the Appendix we show how these numerical results are essentially related to the geometrical structure. It is possible to compare the resulting absorption functions with experimental infrared spectra. To date there is no simple way to unravel the stacking composition of samples (we are presenting it in this study) available in literature. For this reason, we have gathered a number of different experimental measurements without insights into their conformational composition. This collection of data permits us to give an assessment of the quality of the different calculations and, in view of our theoretical results (Section 3.4, Appendix), it works as a testing set for our semi-empirical method (see Section 3.4).

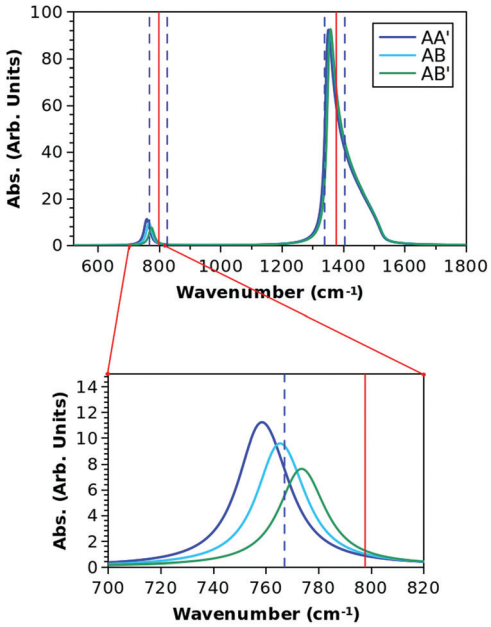

Fig. 6 Calculated vibrational spectra for the three stable h-BN stacking configurations using NC-PBE-TS IFCs and NA parts numerically obtained adopting DFPT at the QE-PAW-PBE level. Red solid vertical lines indicate the average experimental peak values among the six cited ones in Table 3 and blue vertical dotted lines indicate the experimental range (Table 3).

In Fig. 8 and in Table 3, we report the peak frequencies of the IR experimental set. For comparison with the theoretical results we also report the ranges and average values in Fig. 6 and 9. A good agreement of the theoretical and experimental data is noticeable in the values of the larger peak (Peak 2). Concerning the second most intense peak (Peak 1), the frequencies exhibit, instead, systematically lower values with respect to the experimental range. In general, the experimental frequencies show a wide variability (from 767 to 825 cm^{-1} for Peak 1 and from 1338 to 1404 cm^{-1} for Peak 2). Significant trends can be seen among the samples such as sample number 3 presents the lowest values of both peaks. Comparing the two active peaks, among Samples 1, 2 and 3 the whole spectrum shifts homogeneously while Samples 4 and 6 show a different and opposite

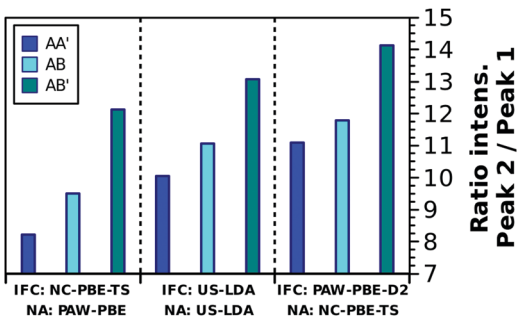

Fig. 7 Calculated ratios between the absorption intensities of the two IR active peaks in the vibrational spectra of the three stable h-BN stacking structures (AA′, AB and AB′) by means of three different theoretical implementations (for PAW-PBE we use Set a, Table TSI of the ESI†).

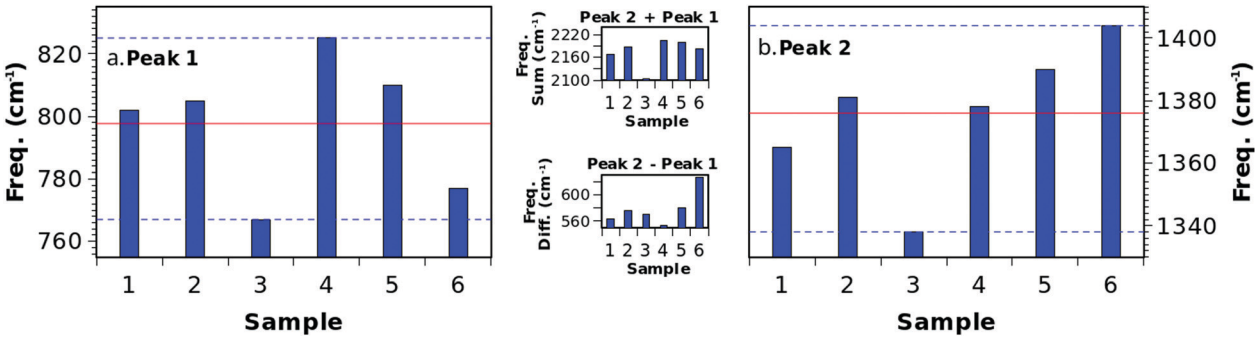

Fig. 8 Experimental peak frequencies from the infrared absorption spectra of bulk and flaked h-BN samples analyzed in the text (references in Table 3). Red horizontal lines indicate the average values. Blue dotted lines enclose the reported experimental range. In the central insets we compare the summed values and differences.

Table 3 Overview of results taken from experimental works concerned with IR spectroscopy in the bulk and flaked h-BN samples. In the third column we report the ratio between the two intensities of the main IR absorption peaks as extrapolated from graphical data. In the fourth and fifth column, the frequencies of the two IR active peaks are given

Label	Source	Ratio	Freq. 1 (cm^{-1})	Freq. 2 (cm^{-1})
Sample 1	Ref. 28	1.805	802	1365
Sample 2	Ref. 29	2.636	805	1381
Sample 3	Ref. 30	1.043	767	1338
Sample 4	Ref. 31	1.282	825	1378
Sample 5	Ref. 32	1.236	810	1390
Sample 6	Ref. 33	1.737	777	1404

order. The anomaly of Samples 4 and 6 is more noticeable when comparing the two central insets in Fig. 8. The distance between the two peaks in different samples is reported in the lower inset, while the sum of the frequencies of the two peaks is reported in the upper inset. This different behaviour of Samples 4 and 6 could arise from a number of factors involving systemic structural deformations deeply affecting the BN planar meshes, *e.g.* ambient temperature, impurities, and other effects produced by nanostructuring processes, the description of which goes beyond the purpose of this work.

In Fig. 10 we report the ratios between the intensities of the two peaks in the referred experimental works. The reported data show a considerable variability, spanning from 2.64 of Sample 2 to 1.04 of Sample 3. Considering the ratios and not just the absolute values enabled us to obtain direct information within an internal standard mechanism.[99] The variability in this parameter is related to structural differences at the atomistic level. Emphasizing this consideration is the complete lack of correlation between the data reported in Fig. 10 and the width of the experimental peaks measured at 1/2 of the peak height (reported in the inset of the same Fig. 10), which instead is affected by the macroscopic features of the specific measured materials (*e.g.* the grain size, which affects the quasiparticle lifetime by being inversely proportional to the probability of surface scattering events).[5,100,101]

The recent work by Amin *et al.*[100] enforces our conclusions, where a first analysis of their results suggests that the ratio between the IR intensities is not due to chemical impurities.

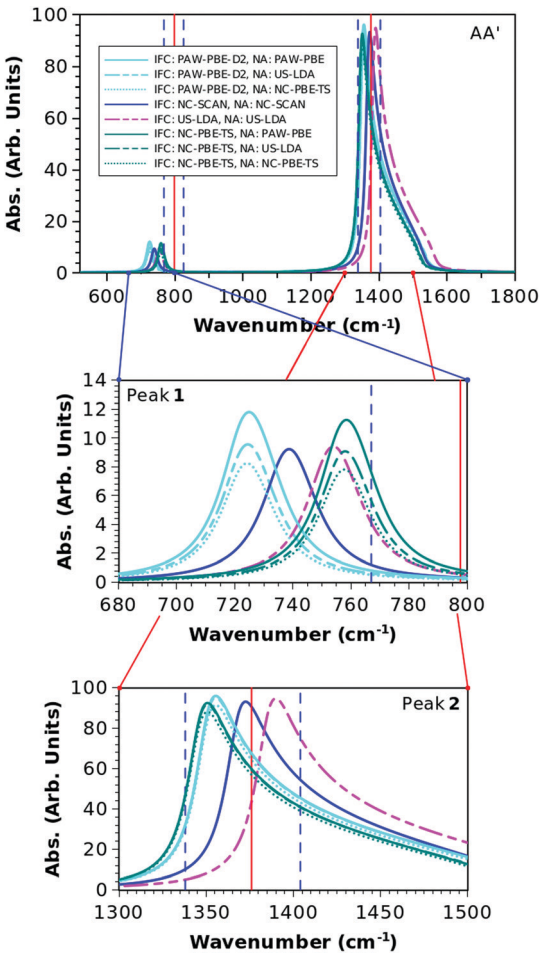

Fig. 9 Vibrational spectra calculated for the AA′ stacking configuration of h-BN with different theoretical approaches, as described in the legend (for PAW-PBE we use Set a, Table TSI of the ESI†). The details of Peak 1 and Peak 2 regions are shown in the insets. Red solid vertical lines indicate the average experimental peak values and blue vertical dotted lines indicate the experimental range limits (among the six spectra in Table 3).

As mentioned before, with the exclusion of the anomalous Samples 4 and 6, the relation between peak values ratios (Fig. 10)

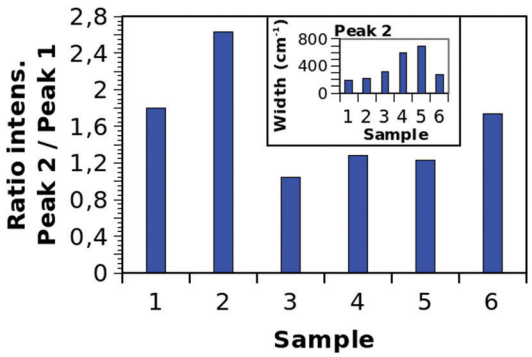

Fig. 10 Experimental ratios between the two main IR absorption intensities in six different experimental measurements performed on bulk and flaked h-BN, taken from the literature and published by independent research groups (Table 3). In the inset: for the same experimental spectra (Table 3), a comparison among the full width at half maximum (FWHM) of the main absorption peak (Peak 2).

and peak frequencies (Fig. 8) is obvious. Samples 2 and 3 show the highest variability. We reasonably hypothesize that the experimental variability (Fig. 8 and 10) is due to different conformational compositions, including the stacking variants, of the referred samples. Following this hypothesis, we deduce that compared with our theoretical results reported in Fig. 6, Sample 2 contains the highest amount of AB′ stacked material in our experimental set, while Sample 3 contains the lowest amount of it.

3.3 Accuracy of the model

In Fig. 9 we report the results of calculated vibrational spectra obtained with different theoretical implementations for the AA′ stacked system. For an easy comparison, the experimental averaged values and range limit lines are shown in the same graphical scheme. Analogous data, calculated for the other two stable variants are reported in the ESI† (Fig. S2 and S4). The agreement between experimental and theoretical values is particularly satisfactory regarding the most intense peak (E_{1u} mode, Peak 2), among all of the considered theoretical perspectives.

The calculated vibrational frequencies of the A_{2u} mode (Peak 1) lie below the lower limit of the experimental range of variability for all employed methods. The presented models underestimate the energy necessary for the A_{2u} vibrational movement (see Fig. 2). As seen in Fig. 9, changing only the NA part of the dynamical matrix does not produce significant changes in the peak frequencies. The differences among the results obtained in the calculated frequencies are mainly attributable to the IFC part.

There are several aspects of the vibrational spectra that indicate the accuracy of the employed method. The first criterion to assess the accuracy is the distance of the frequencies of vibration for the A_{2u} mode (corresponding to Peak 1) from the lower edge of the experimental range (see the Peak 1 enlargement, in the lower part of Fig. 9). In regard to this, the best performance is achieved by the NC-PBE-TS IFC, while the worst results are produced by the PAW-PBE-D2 IFC. A second assessment criterion are the computed intensities of the two IR active peaks. In particular one should consider the ratio between the values of the two peaks,[99] as discussed in Section 3.2.

The gathered experimental values of peak ratios (Fig. 10 and Table 3) span a considerably narrower interval and have a lower average with respect to the calculated ones. *E.g.* with QE-PAW-PBE-D2 IFC, the theoretical range goes from 8.13 (with QE-PAW-PBE NA part) to 11.27 (with NC-PBE-TS NA part). In Fig. 11, we report a wide collection of calculated ratios, using different theoretical approaches for both the IFC and NA parts. From the comparison, it is clear that the main source of variability is the NA part of the dynamical matrix. Analyzing the two inserts of Fig. 9, we notice that the variability in the value of IR active peak ratios, mainly derives from the intensities of Peak 1.

A general consideration of the two assessment criteria shows a substantial failure of the employed methods (DFT with the common dispersion corrections) in the description of the A_{2u} vibrational mode physics. Since the dynamics of this mode reflect predominately the stacking interactions in h-BN, this failure indicates the unsuitability of the model for use in the description of stacking dynamics of our system.

It seems that one method cannot correctly describe both the IFC as well as NA part of the dynamical matrix. This can be shown for the NC-PBE-TS, which delivers the best performance in the calculation of the IFC, while being the worst method in calculating the NA, and *vice versa*, for the PAW-PBE-D2 method.

This is to be expected since it is well known that the GGA methods describe the covalent bonds in a superior way with respect to the LDA methods. We show that LDA exhibits surprisingly good performances in the calculation of phonon frequencies and an average performance regarding the reciprocal intensities of absorption peaks which has also been observed in previous works.[17,40,55,57] US-LDA is a theory of intermediate quality for both assessment criteria. The best results overall were obtained using a complex approach implementing GGA (IFC: NC-PBE-TS, NA: QE-PAW-PBE).

In the Appendix we rigorously show, in an original manner, how the results obtained by varying the theoretical approaches can give dynamical information about the process of charge

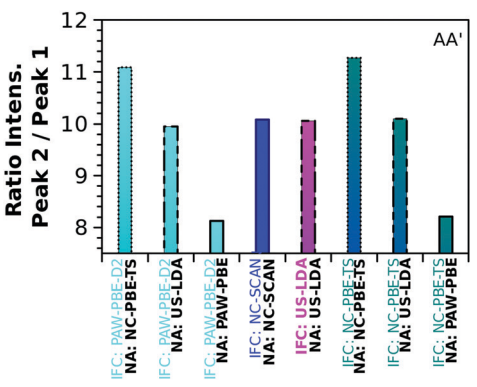

Fig. 11 Calculated ratios between the two IR active absorption intensities in vibrational spectra obtained for the simulated AA′ stacking structure of bulk h-BN with different theoretical implementations (for PAW-PBE we use Set a, Table TSI of the ESI†).

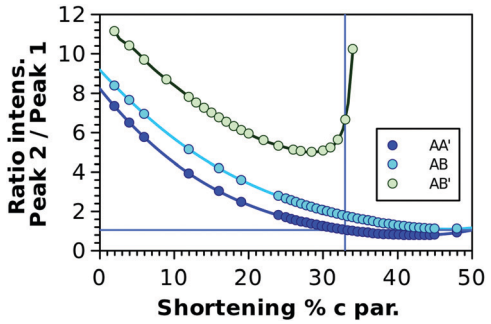

Fig. 12 Calculated ratio between the two IR active absorption intensities for the three stable stacking structures of h-BN reported as functions of the shortening percentage applied to the *c* structural parameters. Each point results from numerical calculation of the relevant NA parameters and IR absorption spectral function. The continuous interpolation lines are calculated by fitting second degree polynomial expressions for AA′ and AB and a twelfth degree polynomial for AB′. The horizontal (blue) line is drawn at 1.043 (Sample 3 of the experimental set). The vertical (blue) line (32.94%) intercepts the horizontal one and the AA′ interpolation line.

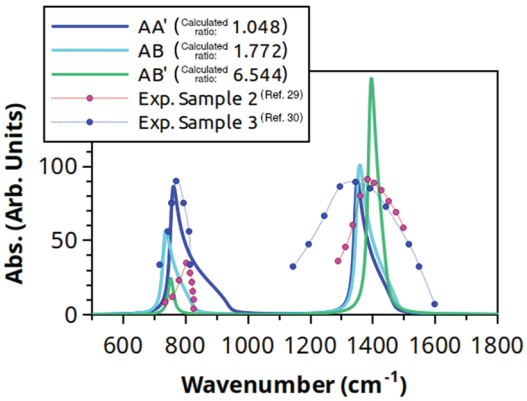

Fig. 13 Vibrational spectra calculated for the three stable stacking structures of h-BN by NC-PBE-TS (for the analytical IFCs) and semi-empirical NA parts of the dynamical matrices obtained with fictitious systems (as explained in Section 3.4). Dotted lines are obtained by graphical extrapolation of selected points from the cited experimental works[29,30] (for these, the measured percentage of absorbance is given, not arbitrary units) and are reported for comparison purposes.

density fluctuation related to the A_{2u} vibrational mode. Following this consideration, we can assert that the effective charge density resulting from the US-LDA calculation (restricting the assertion only to the nitrogen hypothetical polar cones, see the Appendix), is more similar to the "apparent charge density" $\rho_{(Q)}(r)$ of the real system than the one produced by NC-PBE-TS, but less similar to it than the PAW-PBE effective charge density. In this regard LDA is effectively considered to be a well-performing theory. On the other hand, the good performances of LDA also depend on its poor description of the covalent bonds: the underestimation of the bond strengths results in an underestimation of the spring recall forces which compensate the inadequacy of the models to account for the van der Waals stacking interaction.

3.4 Semi-empirical calculation of the dielectric dynamical parameters

The results reported in Fig. 12 are obtained on fictitious systems, which are produced by arbitrary shortening of the *c* structural parameter from the fully optimized structures QE-PAW-PBE-D2 (cell parameters in the ESI† [Table TSII]), without any further geometrical optimization. The figure displays the ratio, calculated between the IR absorption peaks, as a function of the shortening percentage. The data are obtained employing the best performing methods among the tested ones, as discussed in the previous section. The Lorentz broadening functions are always applied separately to each phonon spectral line (Peak 2 is composed by four spectral lines, Peak 1 by one spectral line).

We interpolate the AA′ and AB points with parabolic functions and the AB′ points with a twelfth degree polynomial function. The AB′ function lies systematically above the other two, presenting consistently higher values of ratios. The trend of the AB′ function exhibits an asymptotic behavior at about 35%, making it unreasonable to choose any higher number (at least for the specific AB′ configuration).

As an educated guess, we use, here, the same value of shortening (in percentage, starting from the respective optimized geometries) for the three stable systems. The choice of the shortening is arbitrary and is presented here as a first attempt (expected to be debated in subsequent contributions) to obtain bits of information about the microscopical stacking composition of real samples in a simple way. We propose an optimal shortening of 32.94% of the *c* parameter. The decision comes from the consideration that experimental Sample 3 is purely composed by AA′ stacked material. The chosen value corresponds to the vertical line drawn at the intersection between the AA′ function in Fig. 12 and the Sample 3 horizontal line, in the same figure.

In Section 2.3 we showed how the construction of fictitious systems, with a shortened structural parameter perpendicular to plane directions, permits one to obtain a spatial charge density function more similar to the effective function $\rho_{(Q)}(r)$, at least in the nitrogen polar cones (R_{HP},θ_{HP}). A detailed discussion of these aspects is given in the Appendix.

The real space charge density functions $\rho^{fict}_{(QE\text{-}PAW\text{-}PBE)}(r)$ of these fictitious systems are proposed, here, as the best obtained approximation of $\rho_{(Q)}(r)$ (in the described regions of space). Nitrogen *xz* sections of $\rho^{fict}_{(QE\text{-}PAW\text{-}PBE)}(r)$ and the resulting NA parameters, calculated by numerical implementation of DFPT QE-PAW-PBE, are reported in the ESI† (Fig. S6, S7 and Table TSIV).

The vibrational spectra calculated with these NA parameters and NC-PBE-TS IFC matrices are reported in Fig. 13. The calculated ratios ($Rx_{AA'}$, Rx_{AB} and $Rx_{AB'}$) are reported in the inset of the same figure. Note that the Lorentz broadening functions are always applied separately to each phonon spectral line (*i.e.* Peak 2 is composed by four spectral lines, Peak 1 by only one spectral line). Linear convolutions of these functions can reproduce exactly the experimental lines and the results of this trial calculation are shown in Table 4. Note that, to obtain these values, the IR spectra of Fig. 13 must be shifted in frequency in order to have a correspondence of the peaks. The multiplicative coefficients are reported as calculated frac-

Table 4 Hypothetical compositions of the cited experimental samples, following the premise that Sample 3 is purely composed by AA′ stacked material. With the coefficients in this table, the linear convolution of the three stacking specific spectra reported in Fig. 13 (shifted in frequency in order to superimpose the two peak values) exactly reproduces the experimental results (reported in Column 3)

Label	Source	Exp. ratio	AA′ (%)	AB (%)	AB′ (%)
			HYPOTHESIS		
Sample 3	Ref. 30	1.043	100.00	0.00	0.00
			⇒ **CALCULATION**		
Sample 1	Ref. 28	1.805	30.74	51.00	18.27
Sample 2	Ref. 29	2.636	9.27	51.00	39.73
Sample 4	Ref. 31	1.282	59.29	40.02	0.69
Sample 5	Ref. 32	1.236	66.75	32.53	0.72
Sample 6	Ref. 33	1.737	30.39	55.04	14.56

tions (AA′(%), AB(%) and AB′(%)) of the three different stacking conformations. Again, we point out that these results are based on reasonable (but arbitrary) hypotheses, nevertheless, they show the ease of access of the stacking information with infrared spectroscopy.

The hypothesis that the remarkably low value of intensity ratio between the two IR peaks in Sample 3 is produced by an almost exclusive presence of the AA′ stacking variant means that, in accordance with our dynamical model, we decide to exclude a purely enthalpic behaviour (namely a constant, almost unitary ratio, between the amounts of AA′ and AB variants in all of the samples). An enthalpic description, in fact (*e.g.* applied to Sample 3 : 50% AA′, 50% AB and absence of AB′) would result in a shortening percentage above the asymptote for AB′, contrasting one of our assumptions (the same shortening percentage should be suitable for the three variants). Enthalpic considerations have, nevertheless, been applied in the case of multiple solutions, keeping the fraction of AB′ as the lowest possible.

4 Conclusions

We compared the phononic structures of five possible stacking configurations of bulk h-BN with experimental outcomes (gathered here from literature review). The comparison is based on two distinct criteria: (1) the agreement between the calculated phononic frequencies (of selected vibrational modes, active in infrared or Raman spectroscopy, at $\mathbf{q} = \Gamma$) and the experimental counterparts and (2) the evaluation of the ratio between the intensities of the two IR active peaks.

We provided results for different DFT theoretical implementations, comparing GGA, SCAN and LDA functionals, as well as NC, US and PAW pseudopotential approximations and different treatments of the van der Waals dispersion correction. Differently from what was previously reported by other authors, we obtained better results from GGA functionals rather than from LDA, nevertheless contradictory conclusions with respect to the investigated PP approximations, finding that the FHI Troullier–Martins NC PP implementations produce a better agreement of the eigenvalues with respect to experimental measures, while Kresse–Joubert PAW PP deliver better performances in approaching the experimental order of magnitude regarding the ratios between IR absorption intensities. LDA is presented as a uniform theoretical description, able to sufficiently describe the vibrational properties of bulk h-BN. Here we found, instead, that a complex theoretical approach, based on GGA, better resolves the heterogeneous physics of the examined systems and produces a closer agreement with respect to the experimental numbers. We reported, instead, little or no influence on the results from the different formal treatments of the van der Waals dispersion corrections.

The analysis of the PES surfaces produced by parallel shifting of h-BN planes confirms the stability of the AA′ and AB structures. Besides these, the surrounding area nearby the AB′ symmetry point presents the features of a wide *plateau* and significant dynamical stability for this configuration can be reasonably advanced. An extensive analysis of the energy dispersion schemes for the phononic modes confirmed these hints for stability.

A dynamical stability of the AB′ conformation, variable upon experimental conditions, produces a systematical presence, in different amounts, of this structured material in real samples. This conclusion would theoretically explain the reported wide range of experimental variability for the ratio between the intensities of the two IR active peaks. Our study resulted in a confirmation, never reported before, that the signal from the AB′ stacked variant (ratio between the intensities of the two IR active peaks) is clearly distinguishable and informative. Our results have been directly related to (and confirmed by) purely geometrical considerations (Appendix, see Fig. 15 at a glance), by means of an effective charge density method (called here ''apparent charge density'', citing Cochran and Cowley[70]). We proposed a simple semi-empirical way for the calculation of the non-analytical part of the dynamical matrices (Born Q matrices and dielectric tensors) for layered systems. We showed, presenting a wide amount of theoretical data, that a multifaceted physical approach is necessary and that an effective charge density method could turn out to be the most convenient pathway for it in layered systems.

In view of our theoretical findings, we invite you to consider the possibility that a significant amount of information about the h-BN stacking variability of multilayered real systems could be simply extracted by the exclusive use of infrared spectroscopy and vibrational analysis. An early experimental application of it (very recent) can be found in Harrison *et al.*[99] Due to the lack of theoretical literature on the matter, the cited authors do not fully depict the problem, which is, instead, clearly explainable accounting the results presented here.

As this is a first theoretical effort, it is clear that more extended studies (stacking-specific [peculiar] experimental data sets, validation methods and theoretical models) are expected, to enable any application of these conclusions.

Conflicts of interest

There are no conflicts to declare.

Appendix

Derivation of the dielectric dispersion dynamics from geometry

By the definition of "apparent charge density" given above (Semi-empirical description, Section 2.3) and in view of the obtained numerical results reported in Fig. 11, considering the calculated DFPT $Q_s^{*\alpha\beta}$ and ε as numerical counterparts of the Q matrix elements and $\varepsilon^{(\infty)}$ matrices as defined in the current work (Methods Section 2.1), in a conical system of coordinates centered on the nitrogen nuclei:

$$\begin{aligned} \mathrm{d}x\mathrm{d}y\mathrm{d}z &= \mathrm{d}R\left(\sin\phi\tan\theta\mathrm{d}R + R\cos\phi\tan\theta\mathrm{d}\phi + \frac{R\sin\phi\mathrm{d}\theta}{\cos^2\theta}\right) \\ &\times\left(-R\sin\phi\tan\theta\mathrm{d}\phi + \cos\phi\tan\theta\mathrm{d}R + \frac{R\cos\phi\mathrm{d}\theta}{\cos^2\theta}\right), \end{aligned} \tag{7}$$

it is possible to state, with respect to the nitrogen nuclei, the existence of polar cones of space (R_{PC},θ_{PC}), characterized by:

$$\begin{aligned} &P_{(\text{NC-PBE})}(R_{PC},\theta_{PC}) \le P_{(\text{US-LDA})}(R_{PC},\theta_{PC}) \\ &\le P_{(\text{PAW-PBE})}(R_{PC},\theta_{PC}) \le P_{(Q)}(R_{PC},\theta_{PC}), \end{aligned} \tag{8}$$

where $P_{(x)}(R_{PC},\theta_{PC})$ are integrated charge densities in the fraction of space included in the polar cones. The indices (x) represent the different theoretical methods used to obtain the charge density functions $\rho_{(x)}(R,\theta,\phi)$. θ_{PC} is the conical angle, R_{PC} is the cone height along the z axis and ϕ is the xy planar angle:

$$P_{(x)}(R_{PC},\theta_{PC}) = \iint_{R\le R_{PC},\theta\le\theta_{PC}} \mathrm{d}R\mathrm{d}\theta\int_0^{2\pi}\rho_{(x)}(R,\theta,\phi)\mathrm{d}\phi. \tag{9}$$

$\rho_{(Q)}(R,\theta,\phi)$ is the "effective charge density" as given above.

We plausibly hypothesize the existence of a second type of nitrogen polar cones, which we define by the hypothetical parameters R_{HP} and θ_{HP}, in which:

$$\begin{aligned} &\left[\rho_{(\text{NC-PBE})}(R,\theta,\phi) \le \rho_{(\text{US-LDA})}(R,\theta,\phi) \le \rho_{(\text{PAW-PBE})}(R,\theta,\phi)\right. \\ &\left.\le \rho_{(Q)}(R,\theta,\phi)\right]_{R\le R_{HP},\theta\le\theta_{HP}}. \end{aligned} \tag{10}$$

Stated the properties of the radial solutions of the Schrödinger equation, R_{HP} can be chosen in order to be:

$$\begin{aligned} [R > R_{HP}]_{\theta\le\theta_{HP}} \Rightarrow &\left[\frac{\partial\rho_{(\text{NC-PBE})}(R,\theta,\phi)}{\partial R}\right. \\ &= \frac{\partial\rho_{(\text{US-LDA})}(R,\theta,\phi)}{\partial R} \\ &\left.= \frac{\partial\rho_{(\text{PAW-PBE})}(R,\theta,\phi)}{\partial R}\right]. \end{aligned} \tag{11}$$

In this case R_{HP} is smaller than the atomic radius of nitrogen atom (0.65 Å) and the validity of eqn (10) depends only on the choice of θ_{HP}. A right choice of it implies that the different charge densities reported in Fig. 14, concerning just the part of space included in hypothetical cones (R_{HP},θ_{HP}), approximate different phases of the fluctuation process of the charge density, relevantly to the A_{2u} vibrational mode (Peak 1) in purely crystalline, homogeneously stacked real systems.

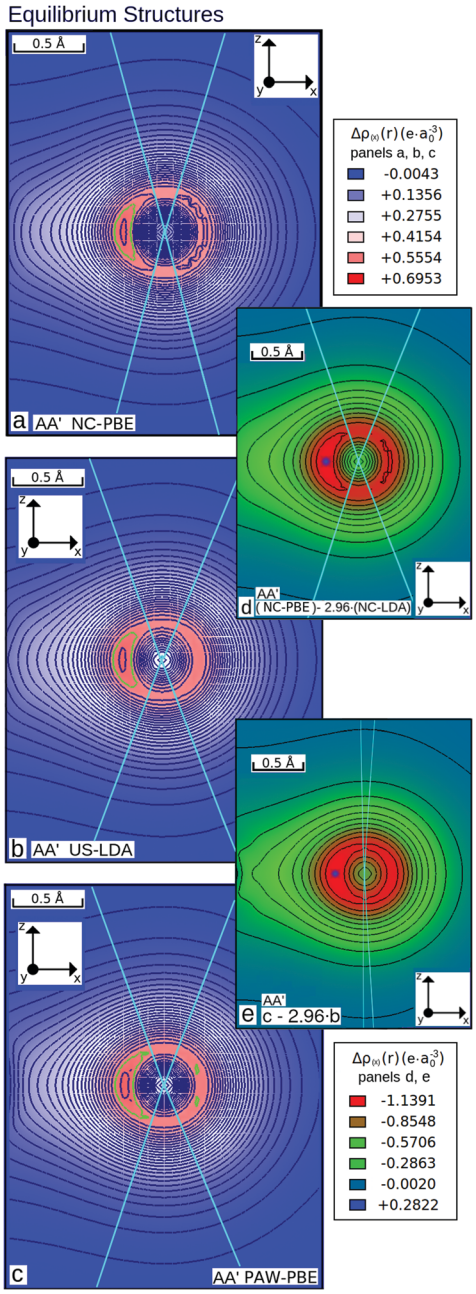

Fig. 14 (a–c) Valence electronic charge density functions (recalculated with a 40 × 30 × 20 Monkhorst–Pack **k**-points grid in the first Brillouin zone of an equivalent orthorhombic unit cell), in the nitrogen xz real plane (atomic centres in the middle of the panels) for the optimized AA′ stacked structure, obtained by means of three different theoretical methods: (a) NC-PBE, (b) US-LDA, (c) PAW-PBE (Set a). In insets (d and e): normalized difference functions between charge densities calculated with different methods as reported in the bottom-left of the panels (where a–c are the functions depicted in the left panels, NC-LDA: PW cutoff 2041 eV for diagonalization, 8163 eV for the charge density). Light blue lines indicate the projections of polar cones in which it is not possible to identify an angular order in the morphological structure of the isoline systems. In Panels a, b and c, the 0.5718 $e\ a_0^{-3}$ isolines of charge density are highlighted in green. Close-up details in the ESI† (Fig. S7).

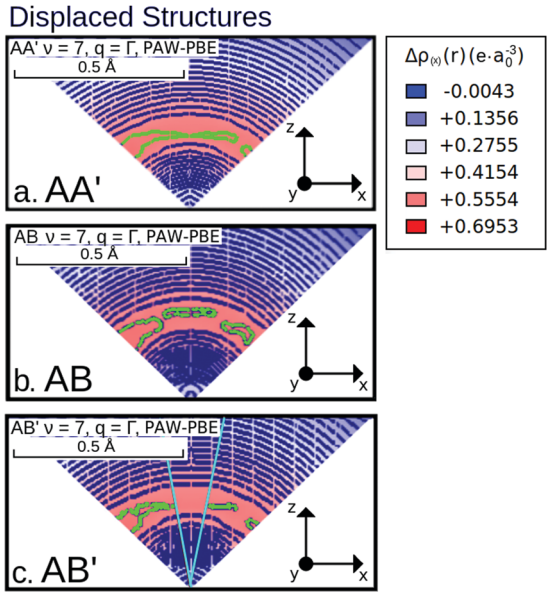

Fig. 15 (a–c) In displaced structures with application of the A_{2u} phononic eigenvectors: valence electronic charge density functions (PAW-PBE [Set a], recalculated with a 40 × 30 × 20 Monkhorst–Pack **k**-points grid in the first Brillouin zone of an equivalent orthorhombic unit cell), in the *xz* real plane sections of polar cones (θ = 45°) with vertex in the centres of the nitrogen atoms. The displaced structures are obtained starting from the relevant (PAW-PBE-D2 [Set a]) optimized (a) AA′, (b) AB, and (c) AB′ layouts and applying displacement vectors as resulting eigenvectors of the structures of Fig. 4 (ν = 7,**q** = Γ). The 0.5718 $e\,a_0^{-3}$ isolines of charge density are highlighted in green, being the most meaningful feature detectable at the depicted level of resolution. In Panel c, light blue lines indicate the projection of a polar cone in which it is not possible to detect an angular structure in the isoline system. The same characteristic cannot be evidenced in the other two structures, as described in the text. Close-up details in the ESI† (Fig. S7).

In Fig. 14 we highlight conical regions in the poles of nitrogen atoms, in which no angular structure is detectable in the reported charge density functions.

An important radial structure can be described (truncated spherical crown, colored in hues of red in all of the panels in Fig. 14) extended from 0.2 to 0.4 Å from the nitrogen nuclei.

Analyzing the difference functions, panels d and e in Fig. 14, we notice that the regions colored in red are the same ones, presenting high values of difference. Stated the polarization of the A_{2u} mode along the *z* axis, it could be easily shown mathematically that the hypothetical cones (R_{HP},θ_{HP}) are contained in the light blue section lines of Fig. 14. In this hypothesis (existence of [R_{HP},θ_{HP}]), the red truncated spherical crowns from 0.2 to 0.4 Å in the polar regions of nitrogen atoms are places of a major charge density variation in the fluctuation movement associated to the A_{2u} vibrational mode (Peak 1).

In Fig. 15, we report, instead, the electronic charge density functions calculated in displaced structures, *i.e.* structures in which displacement vectors have been applied to atoms as resulting from phonon eigenvectors (A_{2u} vibration mode: IR Peak 1, Γ point). A macroscopic difference can be observed among the functions calculated from different stacking geometries. This difference is well depicted from the 0.5718 $e\,a_0^{-3}$ isoline in Fig. 15 (marked in green), and is contained exactly in the highly fluctuating region (red truncated spherical crown from 0.2 to 0.4 Å from nitrogen nuclei) and noticeable in the polar regions of nitrogen atoms (see the light blue conic lines in Panel c, Fig. 15), relating the higher ratio between the IR active absorptions of the AB′ structure (Fig. 7) to simple geometrical considerations.

Acknowledgements

This work was supported by the Czech Science Foundation (18-25128S), the Institution Development Program of the University of Ostrava (IRP201826), the InterAction program (LTAIN19138), and the IT4Innovations National Supercomputing Center (LM2018140).

Notes and references

1 R. Roldán, L. Chirolli, E. Prada, J. A. Silva-Guillén, P. San-Jose and F. Guinea, *Chem. Soc. Rev.*, 2017, **46**, 4387–4399.
2 S. Kumari, R. Gusain and O. P. Khatri, *RSC Adv.*, 2016, **6**, 21119–21126.
3 G. Cassabois, P. Valvin and B. Gil, *Nat. Photonics*, 2016, **10**, 262.
4 M. Kolos and F. Karlický, *Phys. Chem. Chem. Phys.*, 2019, **21**, 3999–4005.
5 H. Henck, D. Pierucci, G. Fugallo, J. Avila, G. Cassabois, Y. J. Dappe, M. G. Silly, C. Chen, B. Gil and M. Gatti, *et al.*, *Phys. Rev. B*, 2017, **95**, 085410.
6 T. C. Doan, J. Li, J. Y. Lin and H. X. Jiang, *Appl. Phys. Lett.*, 2016, **109**, 122101.
7 M. Yankowitz, Q. Ma, P. Jarillo-Herrero and B. J. LeRoy, *Nat. Rev. Phys.*, 2019, **1**, 112–125.
8 J. Serrano, A. Bosak, R. Arenal, M. Krisch, K. Watanabe, T. Taniguchi, H. Kanda, A. Rubio and L. Wirtz, *Phys. Rev. Lett.*, 2007, **98**, 095503.
9 A. Catellani, M. Posternak, A. Baldereschi and A. J. Freeman, *Phys. Rev. B: Condens. Matter Mater. Phys.*, 1987, **36**, 6105.
10 K. T. Park, K. Terakura and N. Hamada, *J. Phys. C: Solid State Phys.*, 1987, **20**, 1241.
11 J. Furthmüller, J. Hafner and G. Kresse, *Phys. Rev. B: Condens. Matter Mater. Phys.*, 1994, **50**, 15606.
12 Y.-N. Xu and W. Ching, *Phys. Rev. B: Condens. Matter Mater. Phys.*, 1991, **44**, 7787.
13 N. Ohba, K. Miwa, N. Nagasako and A. Fukumoto, *Phys. Rev. B: Condens. Matter Mater. Phys.*, 2001, **63**, 115207.
14 L. Liu, Y. Feng and Z. Shen, *Phys. Rev. B: Condens. Matter Mater. Phys.*, 2003, **68**, 104102.
15 G. Constantinescu, A. Kuc and T. Heine, *Phys. Rev. Lett.*, 2013, **111**, 036104.
16 T. Björkman, A. Gulans, A. V. Krasheninnikov and R. M. Nieminen, *Phys. Rev. Lett.*, 2012, **108**, 235502.
17 R. Cuscó, L. Artus, J. H. Edgar, S. Liu, G. Cassabois and B. Gil, *Phys. Rev. B*, 2018, **97**, 155435.
18 N. Marom, J. Bernstein, J. Garel, A. Tkatchenko, E. Joselevich, L. Kronik and O. Hod, *Phys. Rev. Lett.*, 2010, **105**, 046801.

19 J. H. Warner, M. H. Rümmeli, A. Bachmatiuk and B. Büchner, *ACS Nano*, 2010, **4**, 1299–1304.
20 *Joint Committee on Powder Diffraction Standards (JCPDS) - International Center for Diffraction Data, No. 45-0895*, https://www.icdd.com/.
21 *Joint Committee on Powder Diffraction Standards (JCPDS) - International Center for Diffraction Data, No. 73-2095*, https://www.icdd.com/.
22 S. M. Gilbert, T. Pham, M. Dogan, S. Oh, B. Shevitski, G. Schumm, S. Liu, P. Ercius, S. Aloni and M. L. Cohen, *et al.*, *2D Mater.*, 2019, **6**, 021006.
23 G. Ni, H. Wang, B.-Y. Jiang, L. Chen, Y. Du, Z. Sun, M. Goldflam, A. Frenzel, X. Xie and M. Fogler, *et al.*, *Nat. Commun.*, 2019, **10**, 1–6.
24 H. J. Park, J. Cha, M. Choi, J. H. Kim, R. Y. Tay, E. H. T. Teo, N. Park, S. Hong and Z. Lee, *Sci. Adv.*, 2020, **6**, eaay4958.
25 Y. Qi and L. G. Hector Jr, *Appl. Phys. Lett.*, 2007, **90**, 081922.
26 H. Henck, D. Pierucci, Z. Ben Aziza, M. G. Silly, B. Gil, F. Sirotti, G. Cassabois and A. Ouerghi, *Appl. Phys. Lett.*, 2017, **110**, 023101.
27 R. Geick, C. H. Perry and G. Rupprecht, *Phys. Rev.*, 1966, **146**, 543–547.
28 A. Hidalgo, V. Makarov, G. Morell and B. Weiner, *Dataset Pap. Sci.*, 2013, **2013**, 281672.
29 H. E. Çamurlu, S. Mathur, O. Arslan and E. Akarsu, *Ceram. Int.*, 2016, **42**, 6312–6318.
30 A. Mukheem, S. Shahabuddin, N. Akbar, A. Miskon, N. Muhamad Sarih, K. Sudesh, N. Ahmed Khan, R. Saidur and N. Sridewi, *Nanomaterials*, 2019, **9**, 645.
31 L. Chen, H.-F. Xu, S.-J. He, Y.-H. Du, N.-J. Yu, X.-Z. Du, J. Lin and S. Nazarenko, *PLoS One*, 2017, **12**, e0170523.
32 X. Wang, Y. Xie and Q. Guo, *Chem. Commun.*, 2003, 2688–2689.
33 J. Andujar, E. Bertran and M. Polo, *J. Vac. Sci. Technol., A*, 1998, **16**, 578–586.
34 R. J. Nemanich, S. A. Solin and R. M. Martin, *Phys. Rev. B: Condens. Matter Mater. Phys.*, 1981, **23**, 6348–6356.
35 S. Reich, A. C. Ferrari, R. Arenal, A. Loiseau, I. Bello and J. Robertson, *Phys. Rev. B: Condens. Matter Mater. Phys.*, 2005, **71**, 205201.
36 R. Arenal, A. Ferrari, S. Reich, L. Wirtz, J.-Y. Mevellec, S. Lefrant, A. Rubio and A. Loiseau, *Nano Lett.*, 2006, **6**, 1812–1816.
37 L. Museur, E. Feldbach and A. Kanaev, *Phys. Rev. B: Condens. Matter Mater. Phys.*, 2008, **78**, 155204.
38 C. Taylor, S. Brown, V. Subramaniam, S. Kidner, S. Rand and R. Clarke, *Appl. Phys. Lett.*, 1994, **65**, 1251–1253.
39 L. Museur and A. Kanaev, *J. Appl. Phys.*, 2008, **103**, 103520.
40 T. Mosuang and J. Lowther, *J. Phys. Chem. Solids*, 2002, **63**, 363–368.
41 S. Jung, M. Park, J. Park, T.-Y. Jeong, H.-J. Kim, K. Watanabe, T. Taniguchi, D. H. Ha, C. Hwang and Y.-S. Kim, *Sci. Rep.*, 2015, **5**, 1–9.
42 P. Jiang, X. Qian, R. Yang and L. Lindsay, *Phys. Rev. Mater.*, 2018, **2**, 064005.
43 L. Lindsay and D. Broido, *Phys. Rev. B: Condens. Matter Mater. Phys.*, 2012, **85**, 035436.
44 H. Zhou, J. Zhu, Z. Liu, Z. Yan, X. Fan, J. Lin, G. Wang, Q. Yan, T. Yu and P. M. Ajayan, *et al.*, *Nano Res.*, 2014, **7**, 1232–1240.
45 I. Jo, M. T. Pettes, J. Kim, K. Watanabe, T. Taniguchi, Z. Yao and L. Shi, *Nano Lett.*, 2013, **13**, 550–554.
46 S. Lazić, A. Espinha, S. P. Yanguas, C. Gibaja, F. Zamora, P. Ares, M. Chhowalla, W. S. Paz, J. J. P. Burgos and A. Hernández-Mnguez, *et al.*, *Commun. Phys.*, 2019, **2**, 1–8.
47 T. Vuong, G. Cassabois, P. Valvin, V. Jacques, A. Van Der Lee, A. Zobelli, K. Watanabe, T. Taniguchi and B. Gil, *2D Mater.*, 2016, **4**, 011004.
48 J. Wang, Z. Wang, H. Cho, M. J. Kim, T. Sham and X. Sun, *Nanoscale*, 2015, **7**, 1718–1724.
49 C.-J. Kim, L. Brown, M. W. Graham, R. Hovden, R. W. Havener, P. L. McEuen, D. A. Muller and J. Park, *Nano Lett.*, 2013, **13**, 5660–5665.
50 G. J. Slotman, G. A. de Wijs, A. Fasolino and M. I. Katsnelson, *Ann. Phys.*, 2014, **526**, 381–386.
51 L. Wirtz, A. Rubio, R. A. de La Concha and A. Loiseau, *Phys. Rev. B: Condens. Matter Mater. Phys.*, 2003, **68**, 045425.
52 H. Xu, J. Zhou, Y. Li, R. Jaramillo and J. Li, *Nano Res.*, 2019, **12**, 2634–2639.
53 F. Hayee, L. Yu, J. L. Zhang, C. J. Ciccarino, M. Nguyen, A. F. Marshall, I. Aharonovich, J. Vučković, P. Narang and T. F. Heinz, *et al.*, *Nat. Mater.*, 2020, **19**, 534–539.
54 W. Kohn and L. J. Sham, *Phys. Rev.*, 1965, **140**, A1133.
55 I. Hamdi and N. Meskini, *Phys. B*, 2010, **405**, 2785–2794.
56 R. Ahmed, S. J. Hashemifar and H. Akbarzadeh, *et al.*, *Phys. B*, 2007, **400**, 297–306.
57 A. Janotti, S.-H. Wei and D. Singh, *Phys. Rev. B: Condens. Matter Mater. Phys.*, 2001, **64**, 174107.
58 N. Ooi, A. Rairkar, L. Lindsley and J. Adams, *J. Phys.: Condens. Matter*, 2005, **18**, 97.
59 E. Kim and C. Chen, *Phys. Lett. A*, 2003, **319**, 384–389.
60 N. Troullier and J. L. Martins, *Phys. Rev. B: Condens. Matter Mater. Phys.*, 1991, **43**, 8861.
61 G. Kern, G. Kresse and J. Hafner, *Phys. Rev. B: Condens. Matter Mater. Phys.*, 1999, **59**, 8551.
62 W. Yu, W. Lau, S. Chan, Z. Liu and Q. Zheng, *Phys. Rev. B: Condens. Matter Mater. Phys.*, 2003, **67**, 014108.
63 K. Karch and F. Bechstedt, *Phys. Rev. B: Condens. Matter Mater. Phys.*, 1997, **56**, 7404.
64 M. Topsakal, E. Aktürk and S. Ciraci, *Phys. Rev. B: Condens. Matter Mater. Phys.*, 2009, **79**, 115442.
65 J. Sun, R. C. Remsing, Y. Zhang, Z. Sun, A. Ruzsinszky, H. Peng, Z. Yang, A. Paul, U. Waghmare and X. Wu, *et al.*, *Nat. Chem.*, 2016, **8**, 831.
66 J. Sun, A. Ruzsinszky and J. P. Perdew, *Phys. Rev. Lett.*, 2015, **115**, 036402.
67 P. Giannozzi and S. Baroni, in *Handbook of Materials Modeling*, ed. S. Yip, Springer Science & Business Media, 2007, pp. 195–214.
68 E. B. Wilson Jr, *J. Chem. Phys.*, 1941, **9**, 76–84.
69 E. B. Wilson, J. C. Decius and P. C. Cross, *Molecular vibrations: the theory of infrared and Raman vibrational spectra*, Courier Corporation 1980, 1955.
70 W. Cochran and R. Cowley, *J. Phys. Chem. Solids*, 1962, **23**, 447–450.
71 M. Born and K. Huang, *Dynamical theory of crystal lattices*, Clarendon press, 1954.

72 R. M. Pick, M. H. Cohen and R. M. Martin, *Phys. Rev. B: Solid State*, 1970, **1**, 910.

73 P. Giannozzi, S. De Gironcoli, P. Pavone and S. Baroni, *Phys. Rev. B: Condens. Matter Mater. Phys.*, 1991, **43**, 7231.

74 N. Ohba, K. Miwa, N. Nagasako and A. Fukumoto, *Phys. Rev. B: Condens. Matter Mater. Phys.*, 2008, **77**, 129901.

75 X. Gonze and C. Lee, *Phys. Rev. B: Condens. Matter Mater. Phys.*, 1997, **55**, 10355.

76 In our notation $Q^{\star}$ means "uniquely produced numerical Born Q matrix" (with a given numerical method), consistent with a given geometry and ground state electronic charge density distribution function. In the same way ε without indices means "uniquely produced numerical high frequency dielectric tensor".

77 D. Porezag and M. R. Pederson, *Phys. Rev. B: Condens. Matter Mater. Phys.*, 1996, **54**, 7830.

78 P. Giannozzi, S. Baroni, N. Bonini, M. Calandra, R. Car, C. Cavazzoni, D. Ceresoli, G. L. Chiarotti, M. Cococcioni and I. Dabo, *et al.*, *J. Phys.: Condens. Matter*, 2009, **21**, 395502.

79 G. Kresse and J. Furthmüller, *Phys. Rev. B: Condens. Matter Mater. Phys.*, 1996, **54**, 11169.

80 G. Kresse and J. Furthmüller, *Comput. Mater. Sci.*, 1996, **6**, 15.

81 G. Kresse and J. Hafner, *Phys. Rev. B: Condens. Matter Mater. Phys.*, 1994, **49**, 14251.

82 G. Kresse and J. Hafner, *Phys. Rev. B: Condens. Matter Mater. Phys.*, 1993, **47**, 558.

83 G. Kresse and D. Joubert, *Phys. Rev. B: Condens. Matter Mater. Phys.*, 1999, **59**, 1758.

84 P. Hohenberg and W. Kohn, *Phys. Rev.*, 1964, **136**, B864.

85 J. P. Perdew, K. Burke and Y. Wang, *Phys. Rev. B: Condens. Matter Mater. Phys.*, 1996, **54**, 16533.

86 J. P. Perdew, K. Burke and M. Ernzerhof, *Phys. Rev. Lett.*, 1996, **77**, 3865.

87 D. Vanderbilt, *Phys. Rev. B: Condens. Matter Mater. Phys.*, 1990, **41**, 7892.

88 M. Fuchs and M. Scheffler, *Comput. Phys. Commun.*, 1999, **119**, 67–98.

89 D. Hamann, M. Schlüter and C. Chiang, *Phys. Rev. Lett.*, 1979, **43**, 1494.

90 D. Hamann, *Phys. Rev. B: Condens. Matter Mater. Phys.*, 2013, **88**, 085117.

91 D. Hamann, *Phys. Rev. B*, 2017, **95**, 239906.

92 P. E. Blochl, *Phys. Rev. B: Condens. Matter Mater. Phys.*, 1994, **50**, 1795.

93 S. Grimme, *J. Comput. Chem.*, 2006, **27**, 1787–1799.

94 S. Grimme, S. Ehrlich and L. Goerigk, *J. Comput. Chem.*, 2011, **32**, 1456–1465.

95 A. Tkatchenko and M. Scheffler, *Phys. Rev. Lett.*, 2009, **102**, 073005.

96 H. Peng, Z.-H. Yang, J. P. Perdew and J. Sun, *Phys. Rev. X*, 2016, **6**, 041005.

97 A. Togo and I. Tanaka, *Scr. Mater.*, 2015, **108**, 1–5.

98 The IFC matrices are calculated by finite displacements method, with QE-DFT PBE functionals, PAW pseudopotential approximations and Grimme-D2 dispersion corrections, see Table TSI in the ESI.† The NA parts of the dynamical matrices are calculated adopting numerically DFPT PAW-PBE (set *a*, Table TSI, ESI†) effective charges and dielectric tensors.

99 H. Harrison, J. T. Lamb, K. S. Nowlin, A. J. Guenthner, K. B. Ghiassi, A. D. Kelkar and J. R. Alston, *Nanoscale Adv.*, 2019, **1**, 1693–1701.

100 M. S. Amin, T. E. Molin, C. Tampubolon, D. E. Kranbuehl and H. C. Schniepp, *Chem. Mater.*, 2020, **32**, 9090–9097.

101 K. H. Lee, H.-J. Shin, J. Lee, I.-y. Lee, G.-H. Kim, J.-Y. Choi and S.-W. Kim, *Nano Lett.*, 2012, **12**, 714–718.

